








On the Particle Acceleration Mechanisms in a Double Radio Relic Galaxy Cluster, Abell 1240

ARNAB SARKAR ¹, FELIPE ANDRADE-SANTOS ^{2,3}, REINOUT J. VAN WEEREN ⁴, RALPH P. KRAFT ³,
DUY N. HOANG,⁵ TIMOTHY W. SHIMWELL,^{6,4} PAUL NULSEN,^{3,7} WILLIAM FORMAN,³ SCOTT RANDALL ³, YUANYUAN SU,⁸
PRIYANKA CHAKRABORTY,³ CHRISTINE JONES,³ ERIC MILLER ¹, MARK BAUTZ,¹ AND CATHERINE E. GRANT ¹

¹*Kavli Institute for Astrophysics and Space Research, Massachusetts Institute of Technology, 70 Vassar St, Cambridge, MA 02139*

²*Department of Liberal Arts and Sciences, Berklee College of Music, 7 Haviland Street, Boston, MA 02215, USA*

³*Center for Astrophysics | Harvard & Smithsonian, Cambridge, MA 02138, USA*

⁴*Leiden Observatory, Leiden University, PO Box 9513, 2300 RA Leiden, The Netherlands*

⁵*Hamburger Sternwarte, University of Hamburg, Gojenbergsweg 112, 21029 Hamburg, Germany*

⁶*ASTRON, the Netherlands Institute for Radio Astronomy, Oude Hoogeveensedijk 4, 7991 PD Dwingeloo, The Netherlands*

⁷*ICRAR, University of Western Australia, 35 Stirling Hwy, Crawley, WA 6009, Australia*

⁸*University of Kentucky, 505 Rose street, Lexington, KY 40506, USA*

ABSTRACT

We present a 368 ks deep Chandra observation of Abell 1240, a binary merging galaxy cluster at a redshift of 0.195 with two Brightest Cluster Galaxies (BCGs) may have passed each other 0.3 Gyr ago. Building upon previous investigations involving GMRT, VLA, and LOFAR data, our study focuses on two prominent extended radio relics at the north-west (NW) and south-east (SE) of the cluster core. By leveraging the high-resolution Chandra imaging, we have identified two distinct surface brightness edges at ~ 1 Mpc and 1.2 Mpc NW and SE of the cluster center, respectively, coinciding with the outer edges of both relics. Our temperature measurements hint the edges to be shock front edges. The Mach numbers, derived from the gas density jumps, yield $\mathcal{M}_{SE} = 1.49^{+0.22}_{-0.24}$ for the South Eastern shock and $\mathcal{M}_{NW} = 1.41^{+0.17}_{-0.19}$ for the North Western shock. Our estimated Mach numbers are remarkably smaller compared to those derived from radio observations ($\mathcal{M}_{SE} = 2.3$ and $\mathcal{M}_{NW} = 2.4$), highlighting the prevalence of a re-acceleration scenario over direct acceleration of electrons from the thermal pool. Furthermore, we compare the observed temperature profiles across both shocks with that of predictions from collisional vs. collisionless models. Both shocks favor the Coulomb collisional model, but we could not rule out a purely collisionless model due to pre-shock temperature uncertainties.

Keywords: Galaxy cluster — ICM — Shock front — Cosmology

1. INTRODUCTION

Galaxy clusters, the largest gravitationally collapsed structures in the universe, play a vital role in understanding the evolution of cosmic structures. Over time, these clusters grow through the complex processes of gas accretion from large-scale filaments and mergers of smaller clusters and groups (Alvarez et al. 2022; Kraft et al. 2022; Zhang et al. 2023). Such mergers are characterized by prodigious amounts of energy, long lifetimes extending over billions of years, and vast physical scales spanning several Mpc (Markevitch et al. 1999; Sarkar et al. 2022b). During these merger events, a substantial

portion of the released gravitational energy is converted into thermal energy through the generation of shocks and turbulence (Markevitch & Vikhlinin 2007).

However, beyond the thermal component, a lesser fraction ($< 1\%$) of the shock energy might be channeled into the acceleration of cosmic rays (CRs) (Hoang et al. 2018). The presence of magnetic fields in galaxy clusters enables these accelerated CRs to emit synchrotron radiation, which can be detected and studied using radio telescopes (e.g., Jones & Ellison 1991; Ensslin et al. 1998; Cassano et al. 2010; Brunetti & Jones 2014; van Weeren et al. 2019). Radio relics, elongated and arc-like radio sources, have been identified as a prominent signature of cluster merger shocks (e.g., Brunetti et al. 2009; Feretti et al. 2012; de Gasperin et al. 2014; van Weeren

et al. 2016; Inchingolo et al. 2022). Understanding the mechanism responsible for particle acceleration in these low-Mach number cluster merger shocks is a significant challenge.

Despite decades of observations and simulations, the particle acceleration by the merger shock is not yet fully understood. To explain the observed radio relics, two main particle acceleration mechanisms have been proposed: first, shock acceleration – where particles from the thermal pool gain energy through multiple crossings of the shock front via Diffusive Shock Acceleration (DSA; Drury 1983; Markevitch et al. 2005). According to the DSA theory, the efficiency of particle acceleration is expected to be very low for shocks with low Mach number ($\mathcal{M} < 4$). Consequently, the existence of bright radio relics is puzzling within the context of standard DSA (e.g., Markevitch et al. 2005; Kang et al. 2012). On the other hand, re-acceleration theory predicts shocks re-accelerate a population of pre-existing (“fossil”) relativistic electrons via DSA (e.g., Markevitch et al. 2005), bypassing the low acceleration efficiency problem in shock acceleration from the thermal pool. Radio galaxies, commonly found in clusters, serve as good source candidates for these fossil electrons (e.g., van Weeren et al. 2017).

X-ray and radio observations of Abell 3411-3412 provided compelling evidence for particle re-acceleration at cluster merger shocks (van Weeren et al. 2017). The discovery involves the observation of a tailed radio galaxy connected to a radio relic, accompanied by spectral flattening where the fossil plasma intersects with the relic. Galaxy clusters with diametrically opposed double radio relics offer compelling platforms for investigating particle (re-)acceleration on Mpc scales (van Weeren et al. 2011b; Hoang et al. 2018). The spatial arrangement of these double relics, emerging on the major axis of an elongated cluster, points to head-on binary mergers of nearly equal-mass clusters occurring nearly in the plane of the sky (e.g., van Weeren et al. 2011a; Bonafede et al. 2017). This distinctive configuration minimises projection effects and offers a unique setting to explore particle (re-)acceleration without the complexities of relativistic electron mixtures along the line of sight (LOS) (Stroe et al. 2013). Additionally, given the likelihood of mildly relativistic electron seed populations being tied to aged AGN outbursts, the presence of these double relics offers insights into the origin of relics – whether they arise from direct acceleration of thermal pool electrons or from pre-existing fossil plasma within the intracluster medium (ICM) (Hoang et al. 2018; Rajpurohit et al. 2022).

Abell 1240 (A1240 hereafter) is a binary merging galaxy cluster at redshift $z = 0.195$ with a virial radius

of $1.9 h_{70}^{-1}$ Mpc (Barrena et al. 2009). Observations in optical band showed the galaxy clumps are separated in the north-south direction by approximately 1.3 Mpc and may have passed each other 0.3 Gyr ago (Cho et al. 2022). A1240 is a well-studied cluster in radio because of double radio relics that are elongated over ~ 650 kpc (northern relic) and ~ 1250 kpc (southern relic) in the east-west direction (Bonafede et al. 2009), rendering it an excellent candidate for studying shock phenomena. Recent studies by Hoang et al. (2018) presented spectral index maps derived from observations spanning the frequency range of 145 MHz to 3 GHz (using LOFAR at 145 MHz, GMRT at 610 MHz, and JVLA at 2–4 GHz). They estimated shock Mach numbers for both relics to be 2.4 ± 0.1 and 2.3 ± 0.1 . Despite its potential, A1240 remains relatively unexplored in X-rays due to the absence of deep observations from XMM-Newton or Suzaku, and the previously existing Chandra observation lacks the depth required for a comprehensive characterization of the cluster dynamics. The primary goal of this letter is to probe the ICM properties and dynamics of two shock fronts in A1240 using new deep Chandra observations. Table 1 presents all existing Chandra observations of A1240, which were performed with ACIS-I in the aim point.

We adopted a cosmology of $H_0 = 67.8 \text{ km s}^{-1} \text{ Mpc}^{-1}$, $\Omega_\Lambda = 0.692$, and $\Omega_M = 0.308$, which gives a scale of $1'' = 3.346 \text{ kpc}$ at the redshift $z = 0.195$ of A1240. Unless otherwise stated, all reported error bars are at 68% confidence level.

Table 1. Chandra observation log

Obs ID	Filtered Exposure (ks)	Obs Date	PI
4961	51.4	2005-02-05	Kempner
22646	33.6	2020-02-09	Andrade-Santos
22647	23.8	2020-03-09	Andrade-Santos
22720	20.5	2020-03-05	Kraft
22965	32.6	2020-02-22	Kraft
23060	19.8	2020-02-10	Andrade-Santos
23061	24.6	2020-02-27	Andrade-Santos
23145	15.8	2020-02-09	Andrade-Santos
23154	21.8	2020-02-10	Andrade-Santos
23155	16.8	2020-02-11	Andrade-Santos
23165	12.9	2020-02-22	Kraft
23176	24.7	2020-03-02	Andrade-Santos
23180	26.8	2020-03-08	Kraft
23187	30.6	2021-01-08	Andrade-Santos

2. DATA PREPARATION

A1240 was observed with *Chandra* during two epochs, once in February 2005 for 51.4 ks and later in February 2020 – January 2021 for 316 ks divided into 13 observations. This yields a cumulative exposure time of approximately 368 ks (see Table 1 for detailed observation logs). We conducted standard data reduction processes employing CIAO version 4.15 and CALDB version 4.9.4 distributed by the *Chandra* X-ray Center (CXC). We have followed a standard data analyzing thread [§].

All level 1 event files underwent reprocessing with the `chandra_repro` task by incorporating the latest gain, charge transfer inefficiency correction, and filtering out the bad grades. VFAINT mode was used to improve the background screening. Flare-affected periods were detected and removed via the `lc_clean` script, with resultant filtered exposure times documented in Table 1. Employing the `reproject_obs` task, all observations were repositioned to a shared tangent location before being combined. The exposure maps in the 0.5–2.0 keV energy bands were generated using `flux_obs`. To address underexposed detector edges, pixels with less than 15% exposure relative to the combined duration were zeroed.

Point sources were identified using `wavdetect` with a range of wavelet radii between 1–16 pixels. The detection threshold was set to $\sim 10^{-6}$, ensuring fewer than one spurious source detection per CCD. We used blanksky background observations to model the non-X-ray background, emission from foreground structures (e.g., Galactic Halo and Local Hot Bubble) along the observed direction and unresolved faint background sources. The blanksky background files were generated using the `blanksky` task and then reprojected to match the coordinates of the observations. We finally tailored the resulting blanksky background to match the 9.5–12 keV count rates in our observations.

3. RESULTS

We present deep *Chandra* observations of A1240 to investigate the merger shocks and associated radio relics in the cluster.

3.1. Imaging analysis

Figure 1 displays the *Chandra* image of A1240 in the 0.5 – 2 keV energy band, revealing the X-ray emission of the cluster superimposed onto radio contours. The existing shallow X-ray emission exhibits an elongated structure in the north-south direction, indicating a double X-ray morphology, consistent with a slightly asymmet-

ric merger Hoang et al. (2018). Radio observations from the VLA (325, 1400 MHz) have indicated that A1240 experienced a major merger between two subcluster cores, which passed each other in the north-south direction, resulting in two merger shocks currently ahead of each subcluster (Bonafede et al. 2009). These merger shocks are responsible for (re)accelerating electron populations, giving rise to extended radio relics that shine brightly in the radio band. The northern and southern radio relics are located at ~ 900 kpc and 1.1 Mpc from the cluster X-ray center (Hoang et al. 2018). Both relics are extended in the EW direction ($\sim 0.7 - 1.3$ Mpc wide; as seen in Figure 1), perpendicular to the main axis of the X-ray emission, similar to the double relics observed in several other galaxy clusters (e.g., van Weeren et al. 2011b).

Previous *Chandra* observations of A1240 were too shallow (52 ks), hence low signal-to-noise, to properly pinpoint the apparent location of both shock front edges, which is crucial to derive Mach numbers of both shocks (Hoang et al. 2018). With new deep *Chandra* observations, we examine both shock front edges by extracting surface brightness profiles across both edges. Figure 2 shows the resulting radial surface brightness profiles as a function of distance from the A1240 core in the 0.5 – 2keV energy band. The extracted profiles across both shock front edges exhibit shapes consistent with the expected projection of a 3D density discontinuity (e.g., Markevitch et al. 2000; Sarkar et al. 2023; Watson et al. 2023). To further quantify the surface brightness edges, we fit the profiles with a spherically symmetric discontinuous double power-law model projected along the line of sight (l),

$$S_X \propto \int n_e^2 dl, \quad (1)$$

where,

$$n_e(r) \propto \begin{cases} \left(\frac{r}{r_{\text{edge}}}\right)^{-\alpha_{\text{post}}}, & \text{if } r < r_{\text{edge}} \\ \frac{1}{C} \left(\frac{r}{r_{\text{edge}}}\right)^{-\alpha_{\text{pre}}}, & \text{if } r \geq r_{\text{edge}} \end{cases} \quad (2)$$

where $n_e(r)$ is the 3D electron density at a radius r , r_{edge} is the radius of the putative edge, C is the density jump, and α_{post} and α_{pre} are the slopes inside and outside the edge, respectively. Additionally, a constant term was introduced to the model to account for residual background after blank-sky subtraction, and its best-fit value was consistent with zero, indicating successful background elimination.

By projecting the estimated emission measure profiles onto the sky plane and using least-square fitting, we fit the observed surface brightness profiles, varying α_1 , α_2 , r_{edge} , and the C as free parameters. The best-fit surface

[§] <http://cxc.harvard.edu/ciao/threads/index.html>

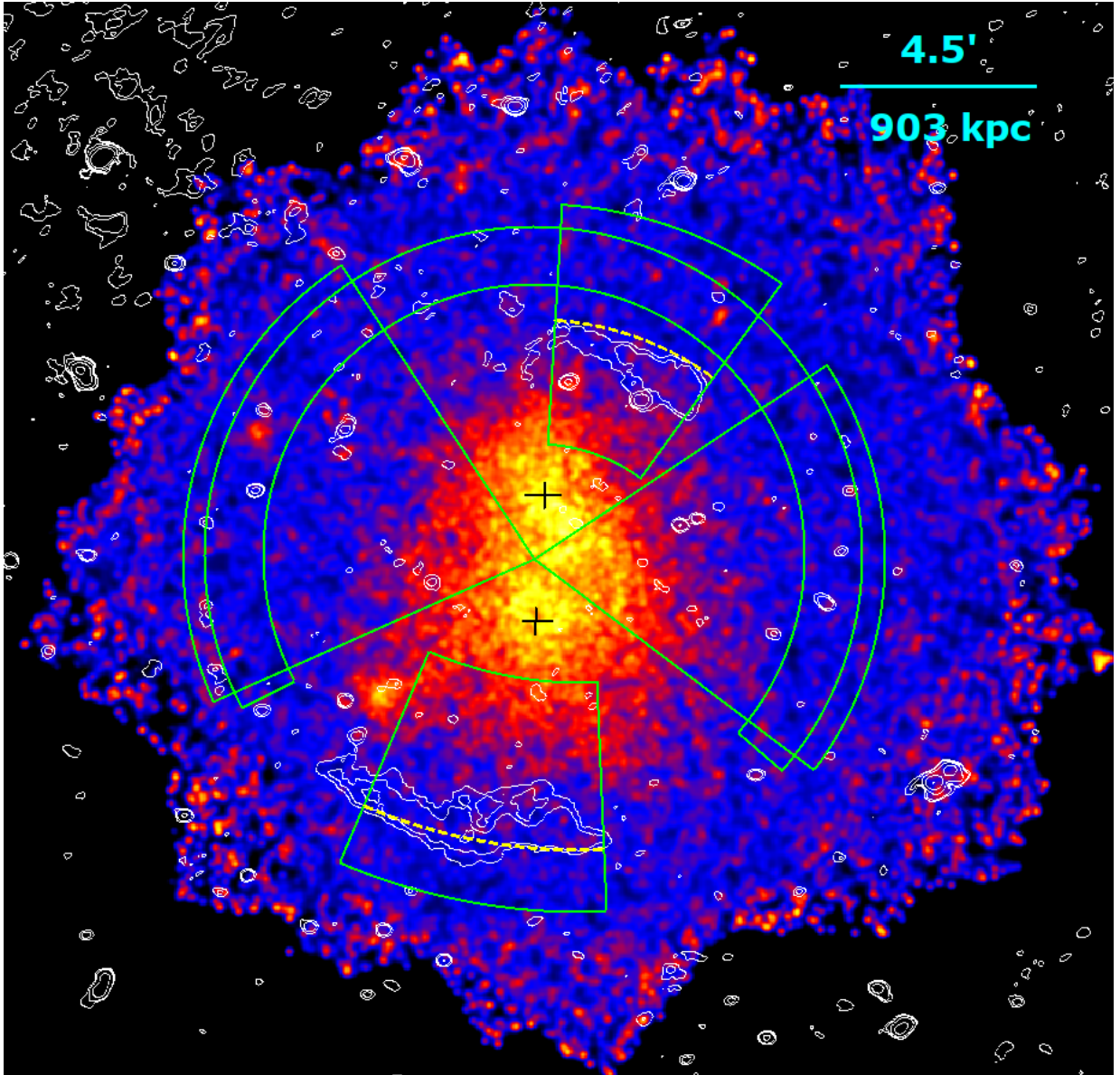


Figure 1. Exposure corrected blanksky-background subtracted *Chandra* image of A1240 in the 0.5–2 keV energy band. Both BCGs are shown in black. White contours show LOFAR 143 MHz radio contours of $[-3, 3, 6, 12, 24, 48] \times \sigma_{\text{rms}}$, where $\sigma_{\text{rms}} = 165 \mu\text{Jy/beam}$, taken from Hoang et al. (2018). Green sectors in NW, SE, and W directions are used for extracting surface brightness and spectral analysis. The yellow dashed curves indicate the positions of shock fronts. The large green annulus running from W, N to E represents the region used for pre-shock temperature measurement.

brightness profiles are shown in Figure 2. The best-fit slopes for the SE edge are $\alpha_{\text{post}} = 2.25 \pm 0.2$, $\alpha_{\text{pre}} = 0.8 \pm 0.1$, and for the NW edge are $\alpha_{\text{post}} = 1.15 \pm 0.3$, $\alpha_{\text{pre}} = 0.7 \pm 0.3$. The electron density jumps by a factor of $\rho_{\text{post}}/\rho_{\text{pre}} = 1.7 \pm 0.3$ ($\chi^2/\text{dof} = 9.2/12$) across the SE edge and $\rho_{\text{post}}/\rho_{\text{pre}} = 1.6 \pm 0.2$ ($\chi^2/\text{dof} = 13/12$), across the NW edge. Assuming these edges represent shock fronts, the derived density jump factors correspond to Mach number of $\mathcal{M}_{\text{SE}} = 1.49^{+0.22}_{-0.24}$ (SE edge) and $\mathcal{M}_{\text{NW}} = 1.41^{+0.17}_{-0.19}$ (NW edge), estimated from the Rankine-

Hugoniot jump condition, defined as

$$\mathcal{M} = \left[\frac{2C}{\gamma + 1 - C(\gamma - 1)} \right]^{\frac{1}{2}}, \quad (3)$$

where $C = \rho_{\text{post}}/\rho_{\text{pre}}$ and for a monoatomic gas $\gamma = 5/3$. We find the location for the SE edge is 1230 ± 50 kpc and 1095 ± 33 kpc for the NW edge from the cluster center. The uncertainties on model parameters are estimated by varying other model parameters freely.

We also extract surface brightness profile along the W direction (from the sector shown in Figure 1) to compare

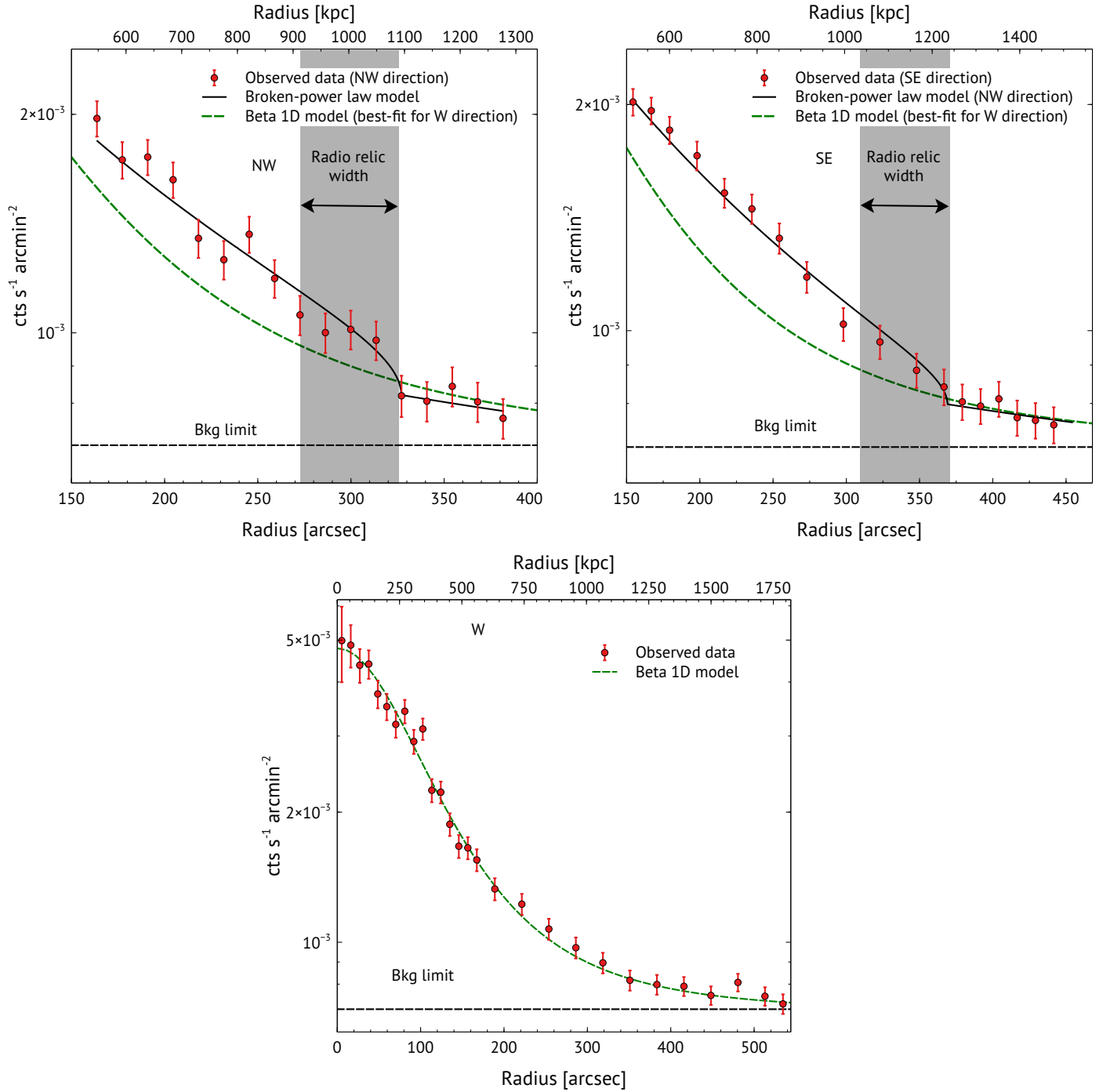


Figure 2. *Top-Left:* Surface brightness profile across the NW relic (red). Black curve shows the best-fit broken powerlaw model. Best-fit electron density is shown in inset. Green dashed curve shows best-fit beta model for the surface brightness profile in the W direction. It is shown here for comparison. The black horizontal dashed line shows the sky + instrument background limit. Grey shaded region represents the width of the relic. *Top-Right:* similar to *Top-Left* but for SE relic. *Bottom:* Surface brightness profile of A1240 extracted from the sector in the W direction. The green dashed curve shows the best-fit 1D- β model, same is shown in *Top-Left* and *Top-Right* panels.

with that of SE and NW directions. Figure 2 (bottom) shows the resulting surface brightness profile in the W direction. We fit this profile with a 1D- β model, as shown in Figure 2. In contrast to the NW and SE directions, no surface brightness discontinuity is found in the W direction, which confirms the north-south axis as the merging direction and potential locations of the shock fronts.

3.2. Spectral analysis

To measure the temperature across both surface brightness edges, we divided the SE and NW sectors (same used for surface brightness profiles) into four regions for each sector. We did the same for the E and W sectors to compare temperatures with that of the temperature across the shock. Each region was carefully chosen to ensure a minimum of ~ 2000 background-subtracted counts in the 0.6 – 7.0 keV energy band. This lower limit was set to guarantee a sufficient number of counts for accurate temperature measurements and to achieve uncertainties within $\sim 30\%$ in the faint pre-shock regions at a 68% confidence level.

For each selected region, we extracted spectra from individual observations and grouped them to contain a minimum of 30 counts per spectral channel. Background spectra were also extracted from the blank-sky event files and subtracted from the source spectra before fitting (Dasadia et al. 2016; Sarkar et al. 2021). The extracted spectra from each region were fitted in XSPEC with an absorbed single-temperature thermal emission model, PHABS \times APEC (Smith et al. 2001). In the spectral fitting process, we fix the redshift to $z=0.195$, and the absorption was set to the Galactic value of $N_{\text{H}} = 2.65 \times 10^{20} \text{ cm}^{-2}$, following Kalberla et al. (2005). The best-fit parameters were obtained by reducing C-statistics (Cash 1979), which provides robust estimates even for spectra with low counts (Chakraborty et al. 2023). To improve the stability of the fitting process, we fixed the metallicity to an typical value of 0.3 (Urban et al. 2017; Sarkar et al. 2022a; Mernier et al. 2023). This choice was made since leaving the metallicity as a free parameter led to poorly constrained results, as observed in previous studies by Russell et al. (2012) and Sarkar et al. (2023). We adopted the solar abundance table of Asplund et al. (2009).

Figure 3 illustrates the best-fit projected temperature profiles in the different directions. We measure temperature across the surface brightness edges in the NW and SE directions. It is evident that the temperature decreases from the cluster center. To isolate the temperature jump attributed to the shock, we also measure temperatures in the W and E directions and compare

them with NW and SE directions. In the NW, SE, and W directions, we observe that the temperature decreases from the cluster center outwards, while the temperature increases from the cluster center in the E direction. Temperature measurements across all radial bins are found to be consistent with each other, except for the third radial bin in the NW and SE directions, where we measure $\sim 2\sigma$ hotter gas compared to the other two directions.

Given the large uncertainties associated with the temperatures from the last radial bins in the SE and NW directions, we opted for a broader approach to measure the pre-shock temperature with smaller uncertainty. We measure the pre-shock temperature from a large circular annulus region around the cluster spanning a radial range of 1.25–1.5 Mpc, as illustrated in Figure 1. The convergence of surface brightness profiles in the NW, SE, and W directions at ≥ 1.25 Mpc from the cluster center, as seen in Figure 2, supports this choice. Moreover, gas temperatures in the NW, SE, W, and E directions at ≥ 1.25 Mpc exhibit consistency within their 1σ uncertainties. These observations collectively indicate uniform ICM properties of A1240 at a radius ≥ 1.25 Mpc in all directions, justifying the selection of a circular annulus around the cluster for pre-shock temperature measurement. We measure a pre-shock temperature of $kT_{\text{pre}} = 2.38 \pm 0.21$ with a $\sim 8\%$ temperature uncertainty (1σ level), which is 2.5 and 3.4 times smaller compared to the pre-shock temperature measurement uncertainties along NW and SE direction.

The temperature jump detected for the NW direction is ~ 1.6 at a 2.5σ significance level and for the SE direction is ~ 1.7 at a 2.7σ significance level. The radial distances of both temperature jumps from the cluster center coincide with the locations of corresponding surface brightness edges. We note that the temperature jump has been measured with respect to the pre-shock temperature measured from the large circular annulus around the cluster. These measurements hint the presence of shock heated gas in the NW and SE directions.

For a shock discontinuity, Rankine-Hugoniot jump conditions relates electron density jump and temperature jump as (Landau & Lifshitz 1959)

$$t = \frac{\zeta - C^{-1}}{\zeta - C}, \quad (4)$$

where $t = T_{\text{post}}/T_{\text{pre}}$ is the temperature jump across the shock front, and $\zeta = (\gamma+1)/(\gamma-1)$. We derive the Mach numbers associated with the above observed temperature jumps by using Equation 3 and 4. For the SE edge, the estimated Mach number is $\mathcal{M}_{\text{SE}} = 1.71 \pm 0.25$, while for the NW edge, $\mathcal{M}_{\text{NW}} = 1.57 \pm 0.34$.

These Mach numbers are consistent with those obtained from surface brightness profiles ($\mathcal{M}_{\text{SE}} = 1.49_{-0.24}^{+0.22}$ and $\mathcal{M}_{\text{NW}} = 1.41_{-0.19}^{+0.17}$). For comparison, we estimate the Mach numbers by considering the temperature jump relative to the last radial bins of the temperature profiles in both NW and SE directions. For SE edge, the estimated Mach number is $\mathcal{M}_{\text{SE}} = 1.62 \pm 0.41$ and for NW edge, $\mathcal{M}_{\text{NW}} = 1.56 \pm 0.52$.

4. ELECTRON HEATING MECHANISM

Shock fronts in galaxy clusters play a pivotal role in redistributing energy and accelerating particles, leading to a variety of observable phenomena. Thus, understanding the thermal behavior behind these shock fronts is crucial for deciphering the underlying physical processes. In this section, we compare the application of two fundamental models, the Coulomb collisional model and the instant-equilibrium model, to investigate the thermodynamics behind a shock front (Markevitch et al. 2005; Russell et al. 2012, 2022).

The Coulomb collisional model, built upon collisional ionization equilibrium assumptions, considers the time-dependent interactions between charged particles in the post-shock region. The Coulomb collisional model predicts when a shock propagates through collisional plasma it heats heavier ions dissipatively within a narrow region of a few ion-ion collisional mean free paths (Spitzer 1962; Sarazin 1988; Etori & Fabian 1998; Markevitch & Vikhlinin 2007). The thermal equilibrium time of the ions among themselves is roughly $\sqrt{(m_p/m_e)} = 43$ times faster than the thermal equilibration time between the electrons and the ions. Thus, the ion kinetic energy that is thermalized by the shock is shared among the ions much more quickly than it is shared with the electrons. Initially, electrons are adiabatically compressed in shocks and later equilibrate with ions through Coulomb scattering, where the equilibration time-scale is governed by (Spitzer 1962; Sarazin 1988),

$$t_{\text{eq}}(e, p) \approx 6.2 \times 10^8 \text{ yr} \left(\frac{T_e}{10^8 \text{ K}} \right)^{3/2} \left(\frac{n_e}{10^{-3} \text{ cm}^{-3}} \right)^{-1} \quad (5)$$

where T_e and n_e are the electron temperature and density, respectively. Electron temperature rises at the shock front via adiabatic compression,

$$T_{e,2} = T_{e,1} \left(\frac{\rho_{\text{post}}}{\rho_{\text{pre}}} \right)^{\gamma-1} \quad (6)$$

where ρ_{pre} and ρ_{post} are the gas density in the pre-shock and post-shock regions. Electron and ion temperatures then subsequently equilibrate via Coulomb collision at

a rate given by,

$$\frac{dT_e}{dt} = \frac{T_i - T_e}{t_{\text{eq}}} \quad (7)$$

where T_i is the ion temperature. Since the total thermal energy density is conserved, the local mean gas temperature, T_{gas} is constant with time, where T_{gas} is given by,

$$T_{\text{gas}} = \frac{n_e T_e + n_i T_i}{n_e + n_i} = \frac{1.1 T_e + T_i}{2.1} \quad (8)$$

where n_i is the ion density, with $n_e = 1.1 n_i$.

Alternatively, instant equilibration model predicts electrons are strongly heated at the shock front, similar to heavier ions, via magnetic fields, hence collisionless heating. The equilibration timescale in the instant heating model is much shorter than t_{eq} and post-shock electron temperature is determined by the Rankine-Hugoniot jump conditions (Markevitch & Vikhlinin 2007).

To compare both model predictions with the observed temperature profile, we estimate post-shock electron temperature from both models using equations 5–8 and projected them along the line of sight using (Etori & Fabian 1998),

$$\langle T \rangle = \int_{b^2}^{\infty} \frac{\epsilon(r) T_e(r) dr^2}{\sqrt{r^2 - b^2}} \bigg/ \int_{b^2}^{\infty} \frac{\epsilon(r) dr^2}{\sqrt{r^2 - b^2}} \quad (9)$$

where $\epsilon(r)$ is the emissivity at physical radius r and b is the distance from the shock front projected onto the sky plane.

Equation 9 gives the emission-weighted temperature, which is the ideal spectroscopic-like temperature if measured with a perfect instrument with flat energy response. In reality, X-ray telescopes do not have flat response. We, therefore, convolve the outcomes of Equation 9 for both models with *Chandra*'s actual response file to predict what we expect to measure. For detailed analysis, we refer readers to Sarkar et al. (2022b). Figure 4 shows the comparison between model predictions and observed temperature profiles of both shocks. Since the pre-shock temperature is the primary source of uncertainty in this measurement, we predominantly use temperature measurement from a large annuli around the cluster as the pre-shock temperature. For both shock fronts, our measurements favor the collisional model over the collisionless model, similar to A2146 (Russell et al. 2022). However, we can not rule out the purely collisionless model due to the large uncertainties in ICM temperature measurements. This prevents us from definitively favoring one model over the other.

5. PARTICLE ACCELERATION MECHANISM

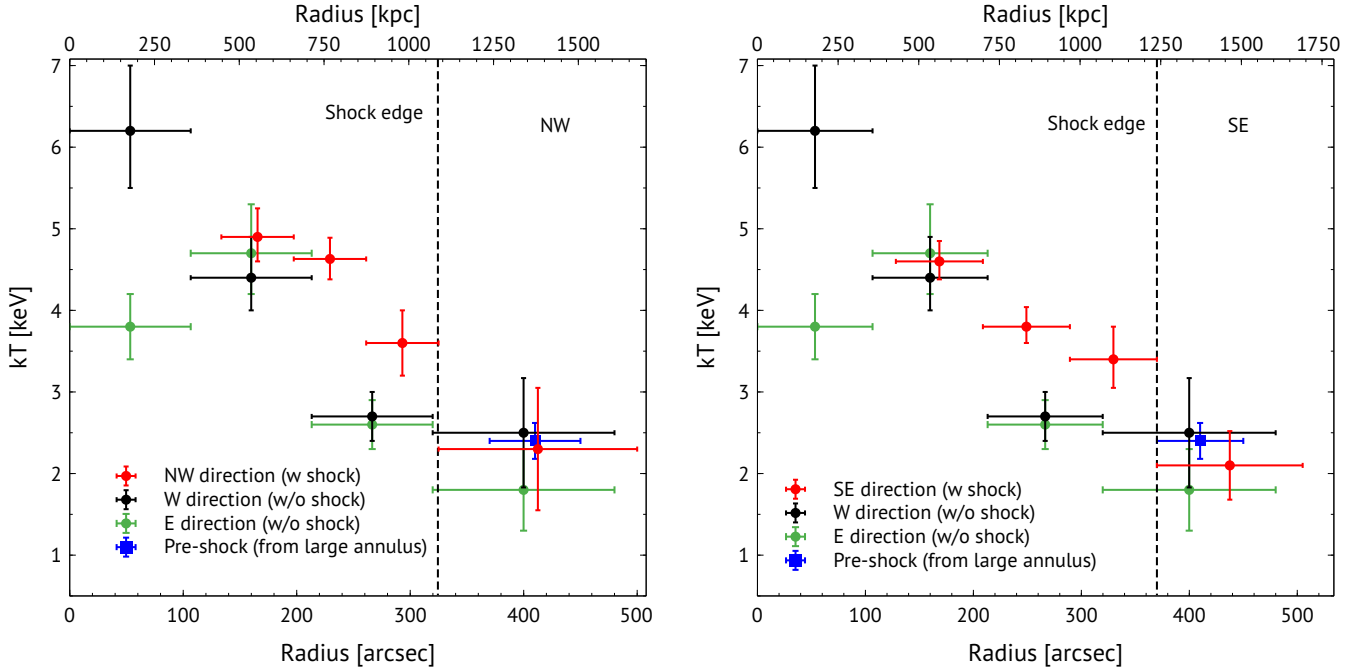


Figure 3. *Top-Left:* Temperature profile across the NW relic (red). Temperature profile along W direction (black) and E (green) direction are plotted for comparison. *Top-Right:* Temperature profile across the SE relic (red). The vertical dashed line represents the location of the shock from the cluster center. In all three figures blue represents the temperature measurement from a large annulus around the cluster, as shown in Figure 1.

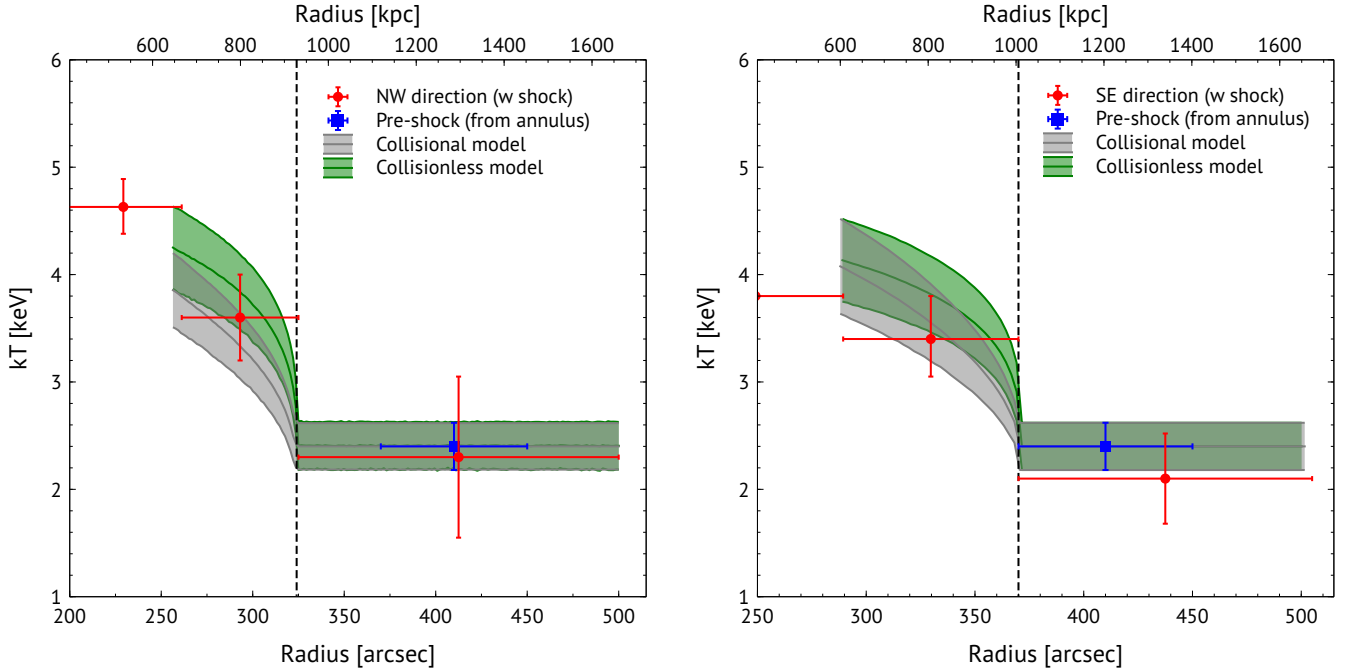


Figure 4. Comparison of the temperature profiles across both shock fronts with the predicted electron temperature profiles based on instant collisionless model (green) and Coulomb collisional model (gray). *Left:* across the NW relic, *Right:* across the SE relic. Both models are only valid for pre and post-shock temperatures only since the model estimations do not include the inherent temperature gradient of the cluster.

Shocks can (re-)accelerate some ICM electrons to relativistic energies, causing them to emit detectable radio emission in the presence of the cluster’s large-scale μG magnetic field (Blandford & Eichler 1987; Feretti et al. 2012; Brunetti & Jones 2014). Merger shocks are often characterized by low Mach numbers, with typical values ranging 1.5–3, as inferred from X-ray observations (Akamatsu & Kawahara 2013). Despite the growing understanding of these processes, the precise efficiency of electron acceleration by low Mach number shocks associated with the radio relics remains an intriguing puzzle (e.g., van Weeren et al. 2017; Botteon et al. 2020). We discuss the implications of our findings in the context of shock acceleration scenarios, specifically focusing on the observed spectral index gradients, discrepancies in Mach numbers between X-ray and radio measurements, and the role of pre-existing fossil plasma.

Two prominent scenarios – direct acceleration of thermal electrons in the ICM and re-acceleration of fossil electrons – have been proposed to explain the origin of relativistic electrons in these shocks. In the acceleration framework, shocks directly accelerate ICM electrons to relativistic energies from the thermal pool. However, the efficacy of direct electron acceleration in weak merger shocks is questioned due to the limited ability of weak shocks to accelerate electrons to relativistic energies. This challenge to the existence of extended radio relics has been highlighted in previous studies (e.g., Kang et al. 2012; Pinzke et al. 2013; Brunetti & Jones 2014; Botteon et al. 2016; Eckert et al. 2016). To address this discrepancy, an alternative re-acceleration scenario has been proposed. In this scenario, low Mach number shocks re-energize a pre-existing population of relativistic electrons rather than directly accelerating thermal electrons. These relic-associated electrons could originate from nearby radio galaxies. Thus, the Mach number measured from radio could be different from that of measured using X-ray in re-acceleration scenario (Bonafede et al. 2014; Shimwell et al. 2015).

Work by Hoang et al. (2018) showed spectral index maps of A1240 derived from observations spanning the frequency range of 145 MHz to 3 GHz (using LOFAR at 145 MHz, GMRT at 610 MHz, and JVLA at 2 – 4 GHz). Both radio relics exhibit spectral index (α) gradients that steepen toward the cluster center, reflecting electron cooling in the post-shock region of outward-traveling shock fronts. Hoang et al. (2018) determined spectral indices of -0.94 ± 0.06 and -0.97 ± 0.05 for the NW and SE shocks, respectively, corresponding to Mach numbers of 2.4 ± 0.1 and 2.3 ± 0.1 . Remarkably, they identified two radio galaxies with redshifts close to the cluster mean redshift (redshifts $z = 0.193$ and 0.192 –

each separated by less than 10 Mpc from A1240), close to the NE relic, which are potentially rich sources in supplying mildly relativistic electrons that contribute to synchrotron radio emission, and one at redshift $z = 0.152$, which is close in projection to the SE relic but separated by more than 100 Mpc from A1240. Peculiar velocities of approximately 500, 750, and 11,000 km s^{-1} would explain the redshift differences, so we can rule out the radio source at $z = 0.152$ as a cluster member. Also, the velocity dispersion in a bound massive cluster stays within a few thousand km/s .

The deep *Chandra* observations allow us to measure Mach numbers more accurately from X-ray surface brightness profiles, providing a crucial comparison with radio-derived Mach numbers. We find significantly lower Mach numbers – $1.41^{+0.17}_{-0.19}$ (for NW shock) and $1.49^{+0.22}_{-0.24}$ (for SE shock) – in contrast to the radio-derived values. Similar discrepancy between X-ray and radio-derived Mach numbers have also been found in works by Skillman et al. (2013), Hong et al. (2015), Roh et al. (2019), Dominguez-Fernandez et al. (2021), and Wittor et al. (2021). Wittor et al. (2021) showed that the radio observations tend to be sensitive to higher Mach numbers, whereas X-ray observations yield an average Mach number for the relic as a whole. This distinction can potentially give rise to variations in the Mach numbers deduced from the two observation methods (Rajpurohit et al. 2022). In addition, a fraction of such disparities could be attributed to projection effects inherent in X-ray surface brightness analysis, a factor that does not significantly influence radio observations. Abell 1240 is a double relic cluster, where two relics are aligned on the sky plane. This spatial arrangement implies that the merger plane is very close to the plane of the sky.

Here, we estimate the required acceleration efficiency (η) for both shocks, assuming the shocks produced the radio relics by accelerating electrons from the thermal pool. The required acceleration efficiency is defined as

$$\eta = \frac{E_{\text{relic}}}{\Delta F_{\text{KE}}}, \quad (10)$$

where E_{relic} is the energy flux of the accelerated relativistic electrons at the relic, defined as, $E_{\text{relic}} = v_{\text{down}} B^2/8\pi$, where v_{down} and B are the the downstream velocity and magnetic field strength. ΔF_{KE} is the available kinetic energy flux at the shock, given by

$$\Delta F_{\text{KE}} = 0.5\rho_{\text{up}}v_{\text{shock}}^3\left(1 - \frac{1}{C^2}\right), \quad (11)$$

where ρ_{up} and v_{shock} are the upstream gas density and shock velocity, respectively, and C is the density compression factor. For the NW and SE shocks, we adopt

pre-shock temperature of 2.3 keV and an upstream electron density of $\sim 10^{-4} \text{ cm}^{-3}$, which results to shock speeds of $v_{\text{shock}} \sim 910 \text{ km/s}$ and 850 km/s . Assuming equipartition of energy, the magnetic field strength is $\sim 2.5 \mu\text{G}$ at the both relic regions (Bonafede et al. 2009; Hoang et al. 2018). For the values presented above, Equation (10) yields a required acceleration efficiency of ~ 1 for both shocks. Achieving such high acceleration efficiency for such low Mach number shocks is challenging for DSA-only acceleration scenario.

Our result strongly suggests that the NW and SE shocks in A1240 did not primarily accelerate electrons from the thermal pool but rather re-accelerated pre-existing relativistic electrons. A similar re-acceleration scenario has been proposed for A3411-3412, demonstrating the broad applicability of this mechanism (van Weeren et al. 2017). The remarkably high efficiency suggests that almost all of the kinetic energy released during the shock goes into the cosmic ray electrons and the magnetic field. Consequently, there is little energy left to increase the temperature of thermal particles. This means we do not anticipate a significant temperature rise across the shock front. However, the substantial uncertainties in the temperature measurements, as seen in Figure 3, leave plenty of latitude in this argument.

6. CONCLUSION

We have presented deep *Chandra* observations of the merging galaxy cluster A1240. Several previous observations in the radio band have shown two extended radio relics in the NW ($\sim 0.7 \text{ Mpc}$) and SE ($\sim 1.3 \text{ Mpc}$) directions with $\sim 2 \text{ Mpc}$ separation between them, highlighting the energetic merging processes. With deep X-ray observations, we have measured the ICM properties across both radio relics. Our measurements, together with the radio observations, provide a multi-wavelength approach in understanding the complex gas dynamics behind shock fronts. We summarize our findings below-

- Shock front edges can primarily be located by using surface brightness profiles. We, therefore, have extracted high-quality surface brightness profiles spanning both radio relics, as depicted in Figure 1. Both profiles are then fitted with broken-powerlaw models to pinpoint the surface brightness edge locations. We have found two distinct surface brightness edges located at 1095 kpc in the NW direction and 1230 kpc in the SE direction from the X-ray center of A1240, notably coinciding with the locations of the radio relics. We have measured the density jumps of $\rho_{\text{post}}/\rho_{\text{pre}} = 1.7 \pm 0.3$ across the SE edge and $\rho_{\text{post}}/\rho_{\text{pre}} = 1.6 \pm 0.2$ across the NW edge.

- Shock fronts are characterized by sharp temperature jumps across the edge. To measure the temperatures across both surface brightness edges, we extracted spectra from the same sectors used for extracting surface brightness profiles in the NW and SE directions. Our ICM temperature measurements showed drops across both the NW (~ 1.6) and SE (~ 1.7) edges ($\sim 2\sigma$ level), hinting the presence of the shock fronts associated with the identified surface brightness edges. Furthermore, a comparative assessment was conducted by comparing the temperature measurements along the NW and SE directions with those of E and W directions. We found within the central $\sim 700 \text{ kpc}$ the ICM temperatures in all directions exhibited remarkable consistency, except for the innermost bin in the E direction. Conversely, the ICM temperatures in the regions just inside the SE and NW edges are found to be hotter at a $\sim 2\sigma$ level compared to other two directions, further supporting the existence of shock-heated gas in the NW and SE directions.

- To understand the electron-heating mode behind shocks, we compared the Coulomb collisional model and instant equilibrium model predictions with the observed temperature profiles across both shocks. Figure 4 illustrates the comparison. Though the temperatures of the post-shock gas for the NW and SE shocks favor the collisional model, we can not rule out either of the models, given the large measurement uncertainties in the gas temperatures.

- Shock Mach numbers derived from X-ray observations in conjunction with the radio measurement provides a unique yardstick in understanding long-debated electron acceleration mechanism by the shocks. The *Chandra* surface brightness profiles provide shock Mach numbers of $\mathcal{M}_{\text{SE}} = 1.49^{+0.22}_{-0.24}$ and $\mathcal{M}_{\text{NW}} = 1.41^{+0.17}_{-0.19}$ for the SE and NW directions, respectively, which are significantly different from the Mach numbers measured from the profiles of the radio spectral index - $\mathcal{M}_{\text{SE}} = 2.3 \pm 0.1$ and $\mathcal{M}_{\text{NW}} = 2.4 \pm 0.1$ (NW). We estimated the required acceleration efficiency of ~ 1 for both shocks. Such high efficiency for such low Mach number shocks strongly indicates that the NW and SE shocks in A1240 re-accelerated pre-existing relativistic electrons rather directly accelerating them from thermal pool.

Our findings underscore the complexities of electron acceleration in weak merger shocks and emphasize the

significance of re-acceleration scenarios. Further investigations, combining multi-wavelength data and sophisticated modeling, are vital to unraveling the intricate mechanisms governing particle acceleration in the dynamic environment of galaxy clusters.

1 We thank anonymous referee for providing helpful com-
 2 ments and suggestions, which improved the paper.
 3 This work is based on observations obtained with the
 4 *Chandra* X-ray Observatory, a NASA mission. This pa-
 5 per employs a list of Chandra datasets, obtained by
 6 the Chandra X-ray Observatory, contained in DOI:
 7 [10.25574/cdc.190](https://doi.org/10.25574/cdc.190). F.A.-S. acknowledges support from
 8 *Chandra* grant GO0-21119X. W.F. acknowledges sup-
 9 port from the Smithsonian Institution, the Chandra
 10 High Resolution Camera Project through NASA con-
 11 tract NAS8-03060, and NASA Grants 80NSSC19K0116,
 12 GO1-22132X, and GO9-20109X.

REFERENCES

- Akamatsu, H., & Kawahara, H. 2013, *PASJ*, 65, 16,
 doi: [10.1093/pasj/65.1.16](https://doi.org/10.1093/pasj/65.1.16)
- Alvarez, G. E., Randall, S. W., Su, Y., et al. 2022, *ApJ*,
 938, 51, doi: [10.3847/1538-4357/ac91d3](https://doi.org/10.3847/1538-4357/ac91d3)
- Asplund, M., Grevesse, N., Sauval, A. J., & Scott, P. 2009,
ARA&A, 47, 481,
 doi: [10.1146/annurev.astro.46.060407.145222](https://doi.org/10.1146/annurev.astro.46.060407.145222)
- Barrena, R., Girardi, M., Boschini, W., & Dasí, M. 2009,
A&A, 503, 357, doi: [10.1051/0004-6361/200911788](https://doi.org/10.1051/0004-6361/200911788)
- Blandford, R., & Eichler, D. 1987, *PhR*, 154, 1,
 doi: [10.1016/0370-1573\(87\)90134-7](https://doi.org/10.1016/0370-1573(87)90134-7)
- Bonafede, A., Giovannini, G., Feretti, L., Govoni, F., &
 Murgia, M. 2009, *A&A*, 494, 429,
 doi: [10.1051/0004-6361:200810588](https://doi.org/10.1051/0004-6361:200810588)
- Bonafede, A., Intema, H. T., Brüggén, M., et al. 2014, *ApJ*,
 785, 1, doi: [10.1088/0004-637X/785/1/1](https://doi.org/10.1088/0004-637X/785/1/1)
- Bonafede, A., Cassano, R., Brüggén, M., et al. 2017,
MNRAS, 470, 3465, doi: [10.1093/mnras/stx1475](https://doi.org/10.1093/mnras/stx1475)
- Botteon, A., Brunetti, G., Ryu, D., & Roh, S. 2020, *A&A*,
 634, A64, doi: [10.1051/0004-6361/201936216](https://doi.org/10.1051/0004-6361/201936216)
- Botteon, A., Gastaldello, F., Brunetti, G., & Kale, R. 2016,
MNRAS, 463, 1534, doi: [10.1093/mnras/stw2089](https://doi.org/10.1093/mnras/stw2089)
- Brunetti, G., Cassano, R., Dolag, K., & Setti, G. 2009,
A&A, 507, 661, doi: [10.1051/0004-6361/200912751](https://doi.org/10.1051/0004-6361/200912751)
- Brunetti, G., & Jones, T. W. 2014, *International Journal of*
Modern Physics D, 23, 1430007,
 doi: [10.1142/S0218271814300079](https://doi.org/10.1142/S0218271814300079)
- Cash, W. 1979, *ApJ*, 228, 939, doi: [10.1086/156922](https://doi.org/10.1086/156922)
- Cassano, R., Ettori, S., Giacintucci, S., et al. 2010, *ApJL*,
 721, L82, doi: [10.1088/2041-8205/721/2/L82](https://doi.org/10.1088/2041-8205/721/2/L82)
- Chakraborty, P., Hemmer, R., Foster, A. R., et al. 2023,
 arXiv e-prints, arXiv:2312.12712,
 doi: [10.48550/arXiv.2312.12712](https://doi.org/10.48550/arXiv.2312.12712)
- Cho, H., James Jee, M., Smith, R., Finner, K., & Lee, W.
 2022, *ApJ*, 925, 68, doi: [10.3847/1538-4357/ac36c8](https://doi.org/10.3847/1538-4357/ac36c8)
- Dasadia, S., Sun, M., Sarazin, C., et al. 2016, *ApJL*, 820,
 L20, doi: [10.3847/2041-8205/820/1/L20](https://doi.org/10.3847/2041-8205/820/1/L20)
- de Gasperin, F., van Weeren, R. J., Brüggén, M., et al.
 2014, *MNRAS*, 444, 3130, doi: [10.1093/mnras/stu1658](https://doi.org/10.1093/mnras/stu1658)
- Dominguez-Fernandez, P., Brüggén, M., Vazza, F., et al.
 2021, *MNRAS*, 500, 795, doi: [10.1093/mnras/staa3018](https://doi.org/10.1093/mnras/staa3018)
- Drury, L. O. 1983, *Reports on Progress in Physics*, 46, 973,
 doi: [10.1088/0034-4885/46/8/002](https://doi.org/10.1088/0034-4885/46/8/002)
- Eckert, D., Jauzac, M., Vazza, F., et al. 2016, *MNRAS*,
 461, 1302, doi: [10.1093/mnras/stw1435](https://doi.org/10.1093/mnras/stw1435)
- Ensslin, T. A., Biermann, P. L., Klein, U., & Kohle, S. 1998,
A&A, 332, 395, doi: [10.48550/arXiv.astro-ph/9712293](https://doi.org/10.48550/arXiv.astro-ph/9712293)
- Ettori, S., & Fabian, A. C. 1998, *MNRAS*, 293, L33,
 doi: [10.1046/j.1365-8711.1998.01253.x](https://doi.org/10.1046/j.1365-8711.1998.01253.x)
- Feretti, L., Giovannini, G., Govoni, F., & Murgia, M. 2012,
A&A Rv, 20, 54, doi: [10.1007/s00159-012-0054-z](https://doi.org/10.1007/s00159-012-0054-z)
- Hoang, D. N., Shimwell, T. W., van Weeren, R. J., et al.
 2018, *MNRAS*, 478, 2218, doi: [10.1093/mnras/sty1123](https://doi.org/10.1093/mnras/sty1123)
- Hong, S. E., Kang, H., & Ryu, D. 2015, *ApJ*, 812, 49,
 doi: [10.1088/0004-637X/812/1/49](https://doi.org/10.1088/0004-637X/812/1/49)
- Inchingolo, G., Wittor, D., Rajpurohit, K., & Vazza, F.
 2022, *MNRAS*, 509, 1160, doi: [10.1093/mnras/stab3096](https://doi.org/10.1093/mnras/stab3096)
- Jones, F. C., & Ellison, D. C. 1991, *SSRv*, 58, 259,
 doi: [10.1007/BF01206003](https://doi.org/10.1007/BF01206003)
- Kalberla, P. M. W., Burton, W. B., Hartmann, D., et al.
 2005, *AAP*, 440, 775, doi: [10.1051/0004-6361:20041864](https://doi.org/10.1051/0004-6361:20041864)
- Kang, H., Ryu, D., & Jones, T. W. 2012, *The Astrophysical*
Journal, 756, 97, doi: [10.1088/0004-637X/756/1/97](https://doi.org/10.1088/0004-637X/756/1/97)
- Kraft, R., Markevitch, M., Kilbourne, C., et al. 2022, arXiv
 e-prints, arXiv:2211.09827,
 doi: [10.48550/arXiv.2211.09827](https://doi.org/10.48550/arXiv.2211.09827)
- Landau, L. D., & Lifshitz, E. M. 1959, *Fluid mechanics*

- Markevitch, M., Govoni, F., Brunetti, G., & Jerius, D. 2005, *ApJ*, 627, 733, doi: [10.1086/430695](https://doi.org/10.1086/430695)
- Markevitch, M., Sarazin, C. L., & Vikhlinin, A. 1999, *ApJ*, 521, 526, doi: [10.1086/307598](https://doi.org/10.1086/307598)
- Markevitch, M., & Vikhlinin, A. 2007, *PhR*, 443, 1, doi: [10.1016/j.physrep.2007.01.001](https://doi.org/10.1016/j.physrep.2007.01.001)
- Markevitch, M., Ponman, T. J., Nulsen, P. E. J., et al. 2000, *ApJ*, 541, 542, doi: [10.1086/309470](https://doi.org/10.1086/309470)
- Mernier, F., Su, Y., Markevitch, M., et al. 2023, arXiv e-prints, arXiv:2310.04499, doi: [10.48550/arXiv.2310.04499](https://doi.org/10.48550/arXiv.2310.04499)
- Pinzke, A., Oh, S. P., & Pfrommer, C. 2013, *MNRAS*, 435, 1061, doi: [10.1093/mnras/stt1308](https://doi.org/10.1093/mnras/stt1308)
- Rajpurohit, K., van Weeren, R. J., Hoeft, M., et al. 2022, *ApJ*, 927, 80, doi: [10.3847/1538-4357/ac4708](https://doi.org/10.3847/1538-4357/ac4708)
- Roh, S., Ryu, D., Kang, H., Ha, S., & Jang, H. 2019, *ApJ*, 883, 138, doi: [10.3847/1538-4357/ab3aff](https://doi.org/10.3847/1538-4357/ab3aff)
- Russell, H. R., McNamara, B. R., Sanders, J. S., et al. 2012, *MNRAS*, 423, 236, doi: [10.1111/j.1365-2966.2012.20808.x](https://doi.org/10.1111/j.1365-2966.2012.20808.x)
- Russell, H. R., Nulsen, P. E. J., Caprioli, D., et al. 2022, *MNRAS*, 514, 1477, doi: [10.1093/mnras/stac1055](https://doi.org/10.1093/mnras/stac1055)
- Sarazin, C. L. 1988, X-ray emission from clusters of galaxies
- Sarkar, A., Su, Y., Randall, S., et al. 2021, *MNRAS*, 501, 3767, doi: [10.1093/mnras/staa3858](https://doi.org/10.1093/mnras/staa3858)
- Sarkar, A., Su, Y., Truong, N., et al. 2022a, *MNRAS*, 516, 3068, doi: [10.1093/mnras/stac2416](https://doi.org/10.1093/mnras/stac2416)
- Sarkar, A., Randall, S., Su, Y., et al. 2022b, *ApJL*, 935, L23, doi: [10.3847/2041-8213/ac86d4](https://doi.org/10.3847/2041-8213/ac86d4)
- . 2023, *ApJ*, 944, 132, doi: [10.3847/1538-4357/acae9f](https://doi.org/10.3847/1538-4357/acae9f)
- Shimwell, T. W., Markevitch, M., Brown, S., et al. 2015, *MNRAS*, 449, 1486, doi: [10.1093/mnras/stv334](https://doi.org/10.1093/mnras/stv334)
- Skillman, S. W., Xu, H., Hallman, E. J., et al. 2013, *ApJ*, 765, 21, doi: [10.1088/0004-637X/765/1/21](https://doi.org/10.1088/0004-637X/765/1/21)
- Smith, R. K., Brickhouse, N. S., Liedahl, D. A., & Raymond, J. C. 2001, *The Astrophysical Journal*, 556, L91, doi: [10.1086/322992](https://doi.org/10.1086/322992)
- Spitzer, L. 1962, *Physics of Fully Ionized Gases*
- Stroe, A., van Weeren, R. J., Intema, H. T., et al. 2013, *A&A*, 555, A110, doi: [10.1051/0004-6361/201321267](https://doi.org/10.1051/0004-6361/201321267)
- Urban, O., Werner, N., Allen, S. W., Simionescu, A., & Mantz, A. 2017, *MNRAS*, 470, 4583, doi: [10.1093/mnras/stx1542](https://doi.org/10.1093/mnras/stx1542)
- van Weeren, R. J., Brüggen, M., Röttgering, H. J. A., & Hoeft, M. 2011a, *MNRAS*, 418, 230, doi: [10.1111/j.1365-2966.2011.19478.x](https://doi.org/10.1111/j.1365-2966.2011.19478.x)
- van Weeren, R. J., Brüggen, M., Röttgering, H. J. A., et al. 2011b, *A&A*, 533, A35, doi: [10.1051/0004-6361/201117149](https://doi.org/10.1051/0004-6361/201117149)
- van Weeren, R. J., de Gasperin, F., Akamatsu, H., et al. 2019, *SSRv*, 215, 16, doi: [10.1007/s11214-019-0584-z](https://doi.org/10.1007/s11214-019-0584-z)
- van Weeren, R. J., Brunetti, G., Brüggen, M., et al. 2016, *ApJ*, 818, 204, doi: [10.3847/0004-637X/818/2/204](https://doi.org/10.3847/0004-637X/818/2/204)
- van Weeren, R. J., Andrade-Santos, F., Dawson, W. A., et al. 2017, *Nature Astronomy*, 1, 0005, doi: [10.1038/s41550-016-0005](https://doi.org/10.1038/s41550-016-0005)
- Watson, C. B., Blanton, E. L., Randall, S. W., et al. 2023, arXiv e-prints, arXiv:2308.04367, doi: [10.48550/arXiv.2308.04367](https://doi.org/10.48550/arXiv.2308.04367)
- Wittor, D., Ettori, S., Vazza, F., et al. 2021, *MNRAS*, 506, 396, doi: [10.1093/mnras/stab1735](https://doi.org/10.1093/mnras/stab1735)
- Zhang, C., Zhuravleva, I., Markevitch, M., et al. 2023, arXiv e-prints, arXiv:2310.02225, doi: [10.48550/arXiv.2310.02225](https://doi.org/10.48550/arXiv.2310.02225)